fire

MDPI

Article

Simulation Analysis of a Spark-Ignition Engine Fueled with Gasoline and Hydrogen

Sebastian Bibiloni-Ipata [1], Santiago Martinez-Boggio [1,*], Simona Merola [2], Adrian Irimescu [2], Facundo Rivoir [1] and Bruno Frankenstein [1]

[1] Instituto de Mecánica y Producción Industrial, Universidad de la República, Av. Julio Herrera y Reissig 565, Montevideo 11300, Uruguay; sbibiloni@fing.edu.uy (S.B.-I.); frivoir@fing.edu.uy (F.R.); bfrankenstein@fing.edu.uy (B.F.)

[2] Sciences and Technologies for Sustainable Energy and Mobility (STEMS), The National Research Council, Via Guglielmo Marconi, 4-80125 Napoli, Italy; simonasilvia.merola@stems.cnr.it (S.M.); adrian.irimescu@stems.cnr.it (A.I.)

* Correspondence: smartinezb@fing.edu.uy; Tel.: +598-97250575

Abstract

The decarbonization of transport demands efficient, low-carbon alternatives to conventional fuels, particularly in regions where full electrification remains constrained. This study investigates the retrofitting of a 1.3 L Geely MR479Q spark-ignition engine for hydrogen operation, combining experimental measurements and one-dimensional numerical simulations in GT-SUITE. The baseline gasoline model was experimentally validated in 12 operating conditions and extended to the full map. In addition, the fuel was changed in the numerical model, and evaluations of hydrogen combustion through predictive sub-models considering mixture formation and pressure-rise limits were performed. Results show that the hydrogen engine operates stably within a wide air–fuel ratio window (λ = 1.0–2.7), with brake thermal efficiencies peaking at approximately 29%, surpassing gasoline operation by up to 5% in the mid-load range. However, port fuel injections cause a reduction in volumetric efficiency and maximum power output due to air displacement, a limitation that could be mitigated by adopting direct injection. A practical hydrogen conversion kit was defined—including injectors, cold-type spark plugs, electronic throttle, and programmable ECU—and the operational cost was analyzed. Economic parity with gasoline is achieved when hydrogen prices fall below ~6 USD kg^{-1}, aligning with near-term green-hydrogen projections. Overall, the results confirm that predictive numerical calibration can effectively support retrofit design, enabling efficient, low-emission combustion systems for sustainable transport transitions.

Keywords: hydrogen combustion; numerical modeling; retrofitting; sustainable transport

Check for updates

Academic Editor: Ali Cemal Benim

Received: 24 November 2025
Revised: 16 December 2025
Accepted: 18 December 2025
Published: 20 December 2025

Copyright: © 2025 by the authors. Licensee MDPI, Basel, Switzerland. This article is an open access article distributed under the terms and conditions of the Creative Commons Attribution (CC BY) license.

1. Introduction

The decarbonization of the transportation sector is one of the most pressing challenges in achieving global climate neutrality [1]. While electrification through battery electric vehicles (BEVs) has become a major pathway, its implementation in certain sectors—such as long-haul transport, agriculture, and developing economies—faces limitations related to energy density, infrastructure, and cost [2]. In this context, the use of hydrogen as an alternative energy carrier for internal combustion engines (H_2-ICEs) represents a transitional yet impactful solution that can leverage existing vehicle platforms and maintenance ecosystems while drastically reducing CO_2 emissions [3].

Hydrogen combustion offers intrinsic environmental advantages, including a zero-carbon exhaust composition and the potential for near-zero particulate matter formation [4]. However, NO_x emissions remain a critical issue, especially under stoichiometric operation [5] or high-load conditions [6]. Modern H_2-ICE concepts, combined with lean combustion strategies and optimized spark timing, have demonstrated thermal efficiencies exceeding 40% [7], approaching those of diesel engines, while maintaining high specific power density [8]. These attributes make hydrogen a viable fuel for the decarbonization of heavy-duty and retrofit applications where fuel cells are economically or technically impractical [9]. There are numerous studies focused on retrofitting conventional gasoline and diesel engines to operate on hydrogen. In the case of engines originally designed for diesel combustion, more substantial modifications are required, such as adjusting the compression ratio, incorporating a spark-ignition system, and implementing other major design changes [10]. Nevertheless, the inherent robustness of diesel engines allows optimization of specific parameters, such as turbocharging pressure, taking advantage of the characteristics typical of these engines [11]. Despite the technical feasibility of retrofitting gasoline engines to hydrogen operation [12], the economic viability of such conversions remains highly dependent on the price of hydrogen [13]. According to recent projections by IRENA [14], the production cost of green hydrogen is expected to decrease from approximately 4–6 USD kg^{-1} in 2025 to below 2 USD kg^{-1} by 2050, driven by improvements in electrolyzer efficiency and reductions in capital cost. This cost evolution directly determines whether hydrogen combustion can compete with conventional fuels in total cost of ownership (TCO) terms, especially for low-volume users and research or fleet-scale retrofits [15].

A major challenge and inherent limitation of hydrogen-fueled engines is the risk of knock and backfire [16]. Although the wide flammability limits of hydrogen allow for a broad operating range through variations in lambda [10], offering advantages such as a trade-off between thermal efficiency and power output. This same operating flexibility, together with the use of port fuel injection (PFI), can also exacerbate both knock and backfire tendencies; therefore, strategies for controlling these phenomena are fundamental [17]. Moreover, the intensity of knock events can be severe enough to damage critical components such as pistons and connecting rods. Therefore, these phenomena must be carefully considered in both the design and retrofit of hydrogen engines to ensure safety, reliability, and practicality. In this context, numerical modeling plays a fundamental role, providing essential insights into combustion behavior [18], emissions formation, and performance, ultimately enabling more robust designs and adaptation strategies.

This work presents a numerical study of a retrofitted spark-ignition engine operating on hydrogen, focusing on the performance and efficiency implications of the conversion and on the fuel price threshold required to achieve economic parity with gasoline. A 1.3 L Geely MR479Q four-cylinder engine was used as the baseline for numerical modeling using a 0D–1D approach implemented in GT-SUITE [19]. The simulation was validated against experimental data for 12 operative gasoline conditions and extended numerically to hydrogen combustion, incorporating limits related to maximum in-cylinder pressure and combustion phasing (BarCAD). The resulting efficiency maps were then coupled with hydrogen cost projections to determine the break-even hydrogen price for comparable operating costs per hour of engine operation. The novel aspect of this article lies in the fact that it focuses on a fully predictive modeling workflow for recalibrating SI engines for hydrogen operation. Also, this study is the first techno-economic analysis of hydrogen retrofits, quantifying the hydrogen price threshold for cost parity, providing a methodology applicable to emerging markets where electrification gaps persist.

2. Materials and Methods

The experimental campaign was performed using a Geely MR479Q four-cylinder, naturally aspirated spark-ignition engine (Zhejiang Geely Holding Group, Ningbo, China) with a total displacement of 1.3 L. The engine features a double overhead camshaft (DOHC) configuration with 16 valves, a compression ratio of 9.5:1, and multi-point port fuel injection. All tests were conducted at the Internal Combustion Engine Laboratory IIMPI, Universidad de la República, Uruguay. The test bench (Figure 1) consists of a hydraulic dynamometer for brake load control (Saenz DS2), an SMAC data-acquisition system (For 0–5 vdc analog sensors, with a frequency of 5 Hz), a programmable ECU (FuelTech FT400) for engine management, and dedicated subsystems for fuel supply, cooling, and exhaust gas evacuation. The engine is coupled to the dynamometer and instrumented with sensors for torque, rotational speed, fuel consumption, air–fuel ratio, and temperature at multiple locations, including coolant, ambient air, and oil, among other variables. Table 1 describes the main specifications of the engine.

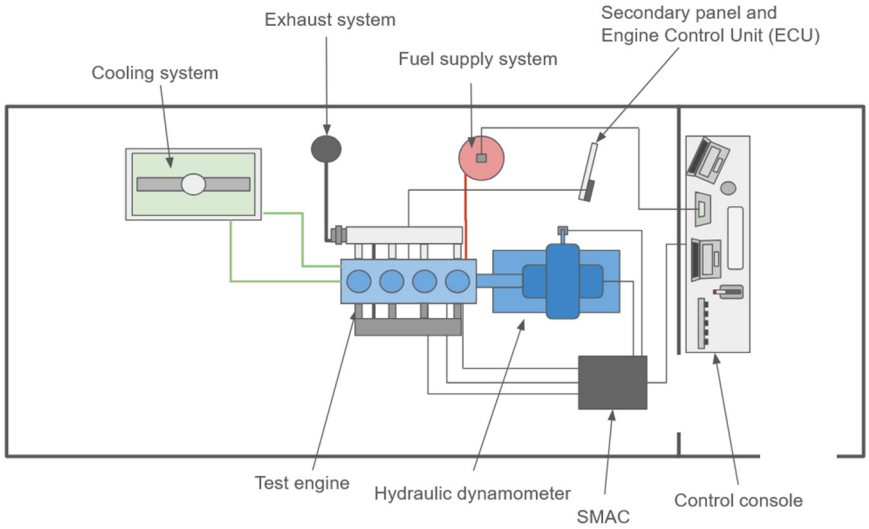


Figure 1. Experimental test bench for Gasoline operation measurements.

Table 1. Engine specifications and fuel used.

Parameter	Unit	Value
Engine type	-	Inline 4-cylinder, naturally aspirated
Displacement	L	1.343
Bore × Stroke	mm	78.7 × 69
Compression ratio	-	9.5:1
Valvetrain	-	DOHC, 16 valves
Fuel system	-	Multi-point port fuel injection (PFI)
Combustion type	-	Spark ignition, Otto cycle
Maximum power	-	63 kW @ 6000 rpm
Maximum torque	-	110 N·m @ 3600 rpm
Cooling system	-	Water-cooled, forced circulation
ECU	-	FuelTech FT400 (programmable)
Dynamometer	-	Hydraulic brake type DS2
Test fuel	-	Gasoline (95 RON); H_2 for retrofit simulations

Engine performance tests with Gasoline were conducted under steady-state conditions, varying speed from 1000 rpm to 3000 rpm and load from 20% to 100% of maximum torque. For each operating point, parameters such as brake power, brake thermal efficiency (BTE), and brake-specific fuel consumption (BSFC) were recorded. The resulting experimental

BSFC map, obtained for gasoline operation, is shown in Figure 2, which served as the validation reference for the numerical model. The map displays BSFC contours as a function of brake mean effective pressure (BMEP) and engine speed, with experimental test points indicated by blue markers.

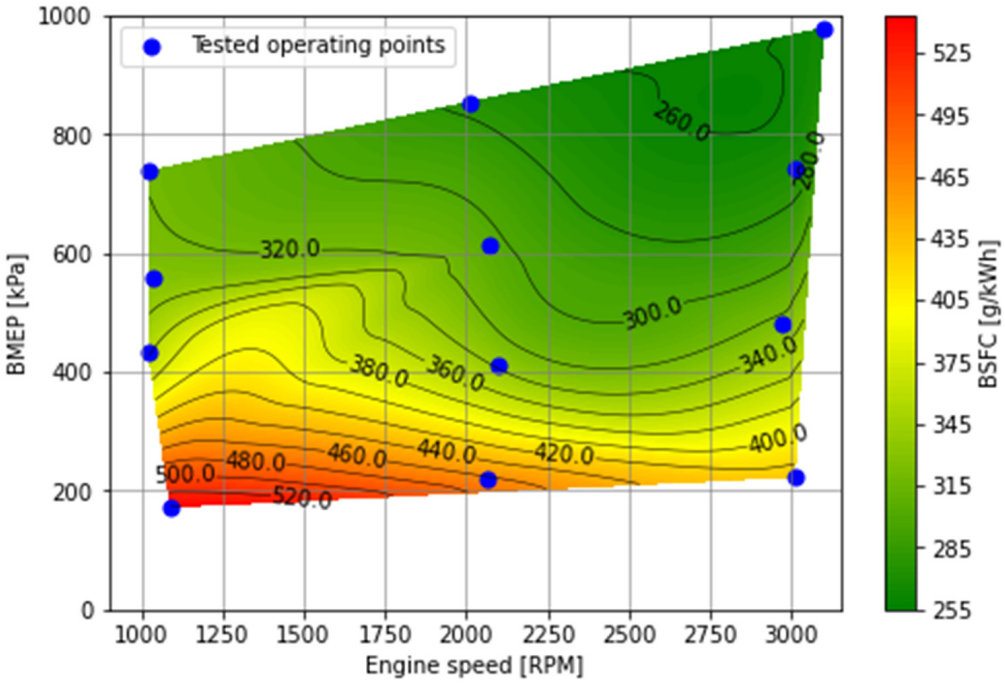


Figure 2. Experimental operational condition measured with Gasoline.

Fuel consumption was determined by continuously measuring the weight of the fuel tank and calculating its variation at each operating point. The uncertainties associated with torque, speed, and fuel consumption measurements were lower than 1.173 N·m, 12 rpm, and 86.9 g/h, respectively, for all evaluated points. Based on a detailed uncertainty-propagation analysis, it was concluded that all points used for model calibration and validation exhibit a percentage uncertainty below 10%, with the vast majority remaining below 5%.

A one-dimensional predictive engine model was developed in GT-SUITE 2025 to reproduce the thermodynamic behavior of the MR479Q engine under both gasoline and hydrogen operation. The model architecture is shown in Figure 3. Each cylinder was represented by a 0D combustion-chamber element [20] coupled with 1D gas-dynamic components modeling [21] the intake and exhaust runners, throttle body, air filter, and catalytic converter. The model incorporates detailed submodels for flow dynamics, heat transfer, and combustion, as well as a predictive formulation for the maximum in-cylinder pressure. The geometric characterization of the intake and exhaust ducts and the cylinder head was carried out using a combination of precision micrometers, an air-flow pressure bench, and 3D scanning techniques. These measurements were used to accurately reproduce the real engine geometry within the quasi-dimensional numerical model [22], ensuring that flow losses and volumetric efficiency were represented as close as possible to experimental conditions [23].

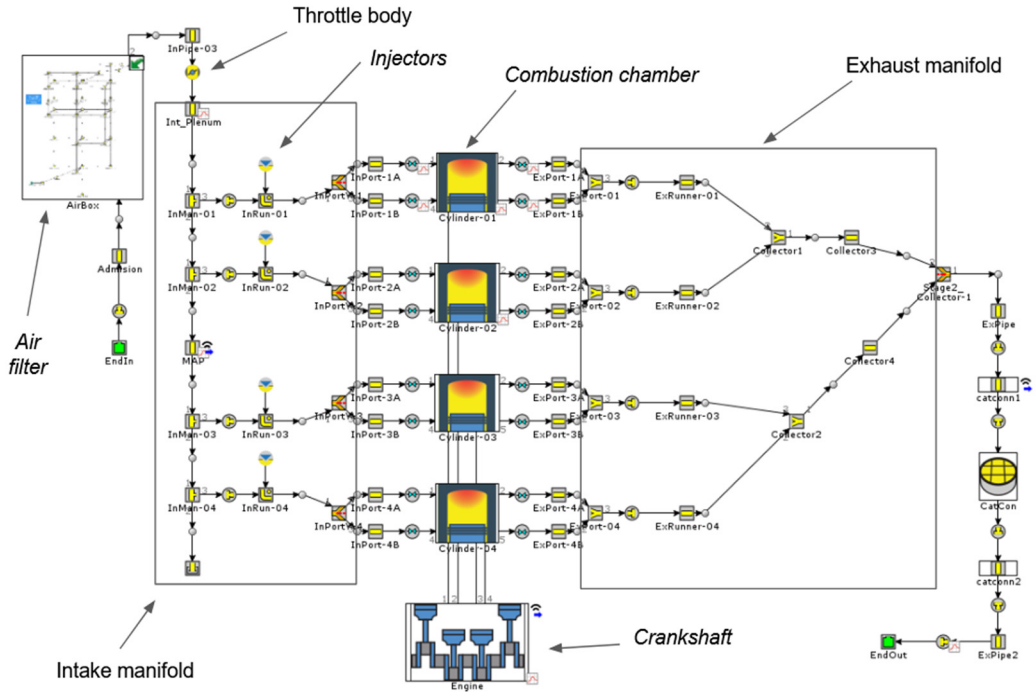


Figure 3. Numerical model for the four-cylinder engine operating under Gasoline and Hydrogen.

The combustion process in the numerical simulations was predicted using the SITurb model, which describes flame propagation in homogeneous charge spark-ignition engines. SITurb is a two-zone formulation that divides the cylinder contents into unburned and burned gas regions [24], enabling the prediction of mass and energy transfer across the flame front as a function of chamber geometry, spark-timing, in-cylinder flow motion, and fuel properties. The rate of entrainment of unburned mixture into the turbulent flame front and the overall mass-burn rate are governed by the following equations:

$$\frac{dM_e}{dt} = \rho_u A_f (S_T + S_L) \tag{1}$$

$$\frac{dM_b}{dt} = \frac{M_e - M_b}{\tau} \tag{2}$$

$$\tau = \frac{L_t}{S_L} \tag{3}$$

where M_e and M_b are the entrained and burned gas masses, respectively. ρ_u is the density of the unburned mixture, A_f is the flame front area, S_T and S_L are the turbulent and laminar flame speeds, τ is the characteristic combustion time and L_t represents the turbulent length scale. Physically, Equation (1) expresses that the unburned mixture is entrained toward the flame front through the area A_f at a velocity equal to the sum of laminar and turbulent flame speeds. Equation (2) links the overall burning rate to the remaining unburned mixture behind the front, while Equation (3) defines the time constant based on the ratio between the Taylor micro-scale and the laminar flame speed [25]. The turbulence intensity and characteristic length scales are obtained from the in-cylinder flow reference object defined in GT-SUITE [26]. During calibration, multipliers are applied to tune the turbulent-flame-speed and Taylor-micro-scale correlations, ensuring that the simulated heat-release rate matches experimental combustion phasing [27]. For the calibration process, a series of experiments were performed for variations in the initial kernel size, the characteristic combustion time, the turbulent length scale, and the piston and cylinder temperatures [28]. The analysis showed that small variations in the initial kernel diameter

and turbulent length scale exerted the strongest influence on combustion duration and peak pressure, whereas wall-temperature adjustments primarily affected heat losses and indicated efficiency. The optimal combination of parameters minimized the deviation between simulated and measured brake torque and BSFC to below 5%, yielding stable and physically consistent flame-propagation behavior across the full operating range.

The final brake specific fuel consumption map obtained for gasoline operation is shown in Figure 4. The contour plot represents the simulated BSFC as a function of engine speed and brake mean effective pressure for the validated MR479Q model. The map exhibits a well-defined efficiency island between 2000 and 3500 rpm and BMEP levels of 900–1100 kPa, where minimum BSFC values of approximately 265 g/kWh were achieved. At lower loads and speeds, BSFC increases gradually due to enhanced friction and heat-transfer losses, while at low-load conditions, the combustion efficiency decreases because of incomplete fuel utilization and throttling effects. The close agreement between the numerical results and experimental data confirms the correct calibration of the flow and combustion submodels. In the model, the air flow is calibrated since the fuel flow is known, and the exhaust gas composition was analyzed. Thus, by measuring the fuel flow and the exhaust gas equivalence ratio, the air flow can be determined. This gasoline BSFC map serves as the baseline reference for subsequent hydrogen simulations, allowing quantitative assessment of efficiency improvements and fuel-consumption reductions after the engine retrofit.

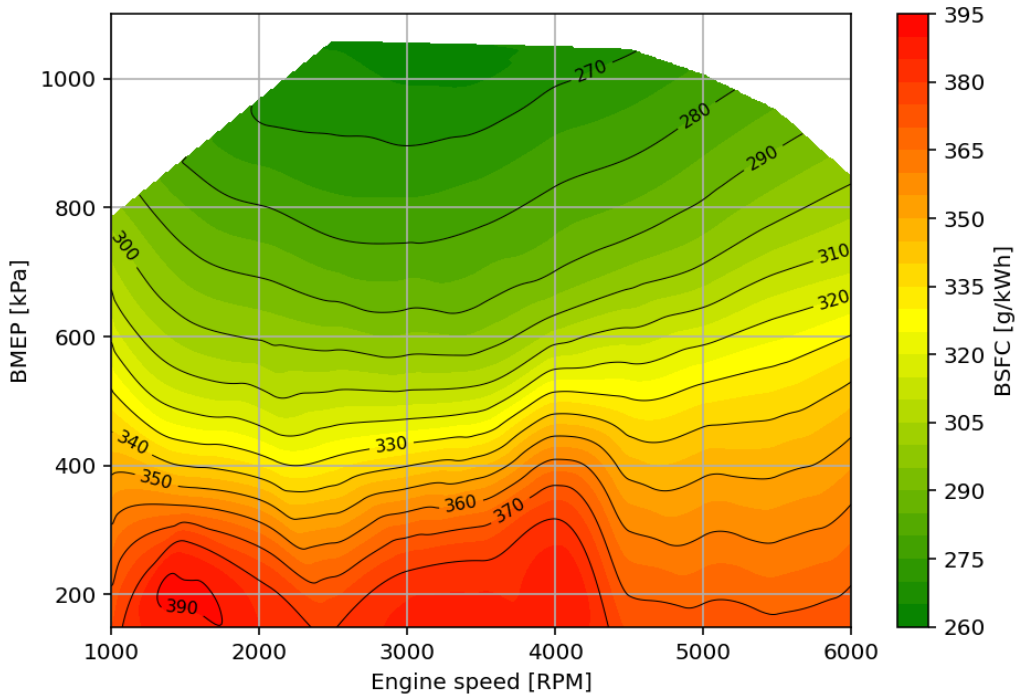


Figure 4. Numerical simulations for Gasoline in terms of fuel consumption.

Although the experimental validation of the gasoline model was carried out in the 1000–3000 rpm range, this speed band represents the region where most automotive SI engines operate during typical driving conditions. Therefore, this range is considered the validated domain of the model. For engine speeds above 3000 rpm, the results presented in this work correspond to simulation-based predictions using the same calibrated set of physical sub-models. Similar approaches have been adopted in several 0D–1D modeling studies where experimental data are available only over a restricted speed range. While these extended-range results should be interpreted with caution, they provide meaningful insight into the expected behavior of the engine at higher speeds, allowing readers to

visualize efficiency, combustion trends, and operational limitations across the full operating envelope up to 6000 rpm. This predictive extension does not replace experimental validation but enhances the practical usefulness of the model for understanding the engine response beyond the validated region.

3. Results and Discussion

This section presents the main results obtained from the hydrogen-engine conversion and subsequent numerical calibration using the validated (gasoline behavior between 1000 and 3000 rpm) MR479Q engine model. The analysis uses predictive simulations to evaluate the combustion and efficiency characteristics of the hydrogen operation, as well as its practical implications in terms of fuel supply and cost. First, the lambda-limit behavior is discussed to identify the operating boundaries imposed by mixture stability. Then, the complete hydrogen evaluation is analyzed, highlighting performance, efficiency, and thermal trends compared with the gasoline baseline. Finally, the implementation of the hydrogen conversion kit and its impact on operational cost are examined to assess the overall technical and economic feasibility of the retrofit.

All hydrogen operating conditions described in this work were obtained through numerical simulations only. No experimental tests with hydrogen were conducted. Accordingly, hydrogen purity is assumed to be 100% in simulations. For internal combustion engines, unlike fuel cells, hydrogen purity has no significant influence on combustion characteristics, provided contaminants remain below typical industrial thresholds.

3.1. Lambda Limit Operation

The hydrogen combustion model was used to determine the operational lambda boundaries of the retrofitted engine. These limits define the range of air–fuel ratios that ensure stable and safe combustion while maintaining acceptable efficiency and avoiding mechanical stress. Two complementary analyses were carried out: (i) the determination of the maximum lambda value (lean-limit operation), and (ii) the identification of the minimum lambda value (near-stoichiometric limit) constrained by in-cylinder pressure and BarCAD criteria.

Figure 5 summarizes the hydrogen combustion operating limits obtained from the numerical simulations. The blue curve represents the maximum lambda (lean limit), while the red curve corresponds to the minimum lambda (rich limit) established by the in-cylinder pressure and BarCAD constraints. The shaded region between them indicates the stable operating envelope where combustion remains efficient and mechanically safe. At low engine speeds, hydrogen combustion remains stable up to approximately $\lambda \approx 2.7$, but as rotational speed increases, the maximum admissible lambda decreases to about $\lambda \approx 2.4$ at 6000 rpm due to reduced mixture residence time and increased turbulence dissipation. To determine this maximum lambda limit, the main criterion was that, at the optimum spark timing, the unburned hydrogen combustion products would not exceed 2% of the injected amount. This ensures that the engine operates in a stable and safe manner, with a fully developed combustion process. Conversely, the minimum lambda remains near 1.15 at low speeds and approaches $\lambda \approx 1.0$ at high rpm, limited by the rapid pressure-rise rate and maximum in-cylinder pressure. The defined region therefore represents the feasible operating window of the converted hydrogen engine, balancing combustion stability, efficiency, and component durability across the entire speed range.

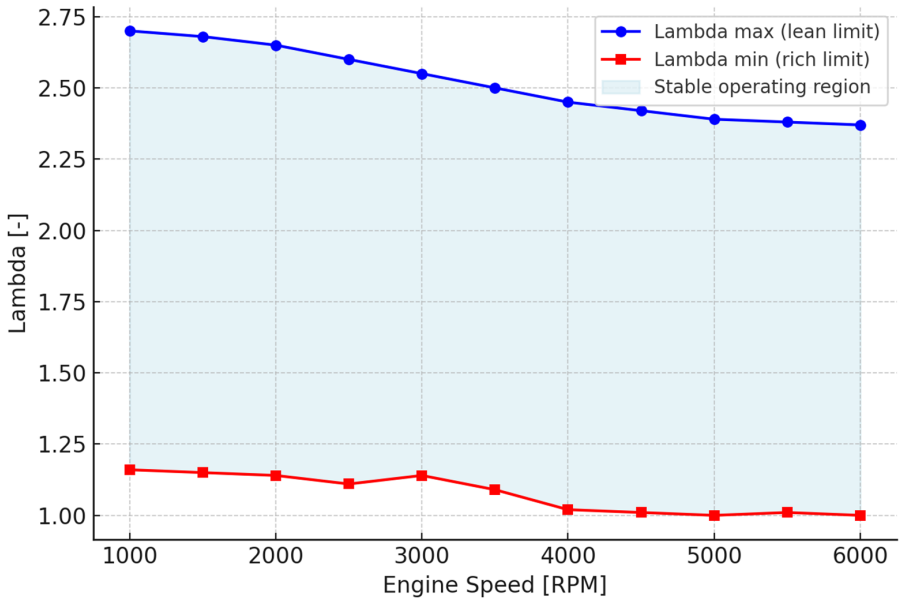
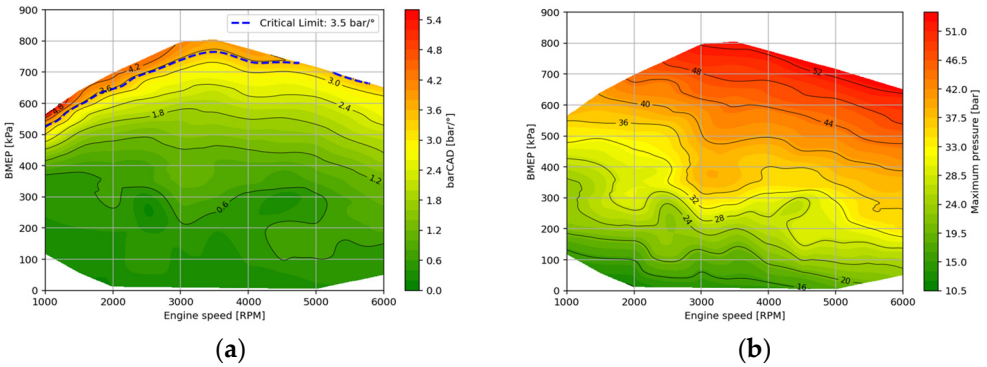


Figure 5. Hydrogen combustion operating limits as a function of engine speed.

Figure 6 illustrates the numerical evaluation of in-cylinder combustion dynamics for hydrogen operation. For this analysis, the in-cylinder behavior was also examined in the gasoline model, which was validated using experimental results. Based on this, the critical points that should not be exceeded on the hydrogen model to avoid surpassing the mechanical stress limits of the engine were identified. Figure 6a presents the distribution of the BarCAD parameter (pressure rise rate, in bar/°CA) as a function of engine speed and load. The dashed blue line marks the maximum allowable limit of 3.5 bar/°CA, adopted to prevent excessive pressure gradients that could lead to mechanical stress or knock-like phenomena. As engine load and speed increase, BarCAD grows exponentially, particularly above 4000 rpm and 700 kPa BMEP, delineating the upper boundary of safe operation. Figure 6b shows the corresponding maximum in-cylinder pressure map, where values remain below the 63 bar threshold established from gasoline-engine reference conditions. This confirms that, under optimal ignition advance and within the acceptable BarCAD region, hydrogen combustion does not impose critical mechanical risks. Together, these maps define the pressure-based criteria used to determine the minimum admissible lambda in Figure 5, ensuring the hydrogen conversion operates safely while maintaining efficient combustion across the speed–load range.



(**a**) (**b**)

Figure 6. Pressure-based constraints for defining the minimum admissible lambda during hydrogen operation. (**a**) Map of the BarCAD parameter as a function of engine speed and load, showing the 3.5 bar/°CA safety limit. (**b**) Map of maximum in-cylinder pressure, with values remaining below the 63 bar mechanical threshold.

3.2. Simulation-Based Hydrogen Calibration and Predicted Performance

Once the admissible lambda limits were established, a full calibration was conducted to characterize the hydrogen operation of the retrofitted SI engine. Figure 7 presents the resulting lambda map obtained from the numerical model, showing the relationship between the air–fuel ratio, engine speed, and load. The distribution of lambda values follows the expected trend for port-fuel-injected hydrogen combustion: lean operation dominates most of the map ($\lambda \approx 1.8$–2.6), while near-stoichiometric conditions are only reached at high load. The contour lines of the throttle position (blue) indicate that air-flow control plays a significant role in regulating torque at low loads, since hydrogen fueling is already limited by the mixture's wide flammability range and the unburned hydrogen combustion products.

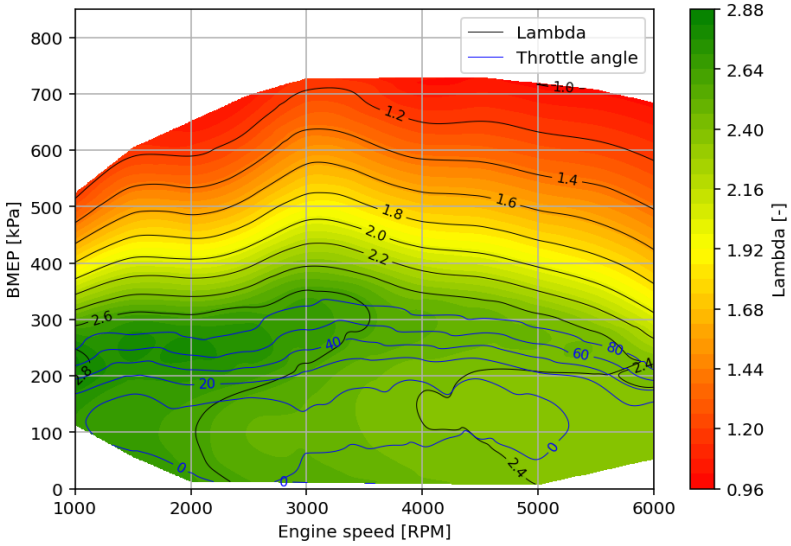
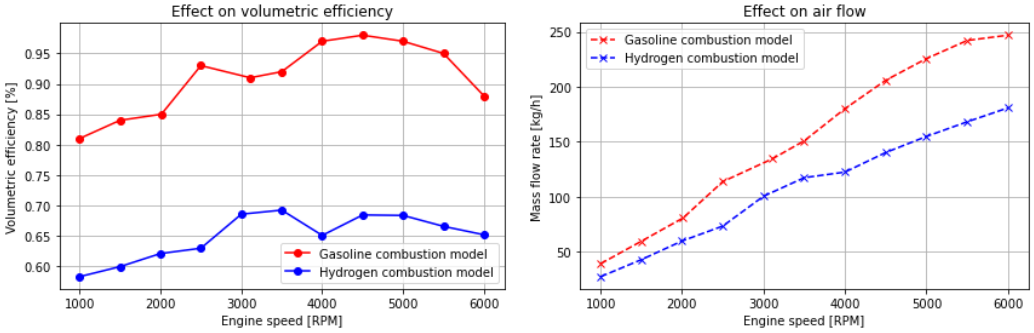


Figure 7. Predicted lambda map of the hydrogen-fueled engine from the calibrated GT-SUITE model, showing air–fuel ratio and throttle angle contours as functions of engine speed and BMEP.

The volumetric and airflow behavior for both gasoline and hydrogen operation are compared in Figure 8a,b. A noticeable decrease in volumetric efficiency is observed for the hydrogen configuration, mainly due to the displacement of intake air by the gaseous fuel and the lower intake density at equivalent manifold pressures. This reduction, approximately 25–30% across the speed range, directly impacts the achievable brake mean effective pressure at high loads. Similarly, Figure 8b shows that the total air mass flow rate in hydrogen operation is consistently below that of gasoline, following the same trend as the volumetric efficiency curve.



(**a**) (**b**)

Figure 8. Comparison between gasoline and hydrogen operation: (**a**) volumetric efficiency versus engine speed; (**b**) intake air mass-flow rate.

This limitation is intrinsic to PFI systems, where hydrogen is mixed with air before entering the combustion chamber, thereby reducing the effective air charge. In contrast, Direct Injection (DI) of hydrogen could mitigate this penalty by introducing the fuel directly into the cylinder after intake valve closure, avoiding displacement of intake air and improving both volumetric efficiency and power output. Despite the inherent penalization in volumetric filling, the hydrogen combustion process remains stable and controllable over the entire operating range. The calibrated model thus reproduces realistic torque and efficiency trends, enabling its later use to assess the brake thermal efficiency and fuel consumption maps, as well as the economic implications of hydrogen fueling, discussed in the following section.

Figure 9 compares the predicted brake thermal efficiency of the hydrogen-fueled MR479Q engine with the baseline gasoline configuration. In Figure 9a, the brake thermal efficiency map obtained from the calibrated hydrogen model shows efficiency values peaking near 29%, particularly in the mid-load and medium-speed range (2000–3500 rpm). Despite the known volumetric-efficiency penalty associated with port-fuel-injected hydrogen, the overall thermal performance is superior to gasoline operation wherever the engine can sustain stable lean combustion. Since experimental hydrogen tests were not available for model validation, the numerical results, such as BTE, were compared with experimental data from similar operating conditions reported for comparable engines, such as [29,30]. This comparison indicates that the numerical model results are reasonable and consistent with the literature. When comparing engines for this type of analysis, parameters such as compression ratio, number of valves, injection system, and aspiration method are essential. However, the cases found in the literature present very similar characteristics, making the available experimental results comparable to those of the model and therefore supporting its validation.

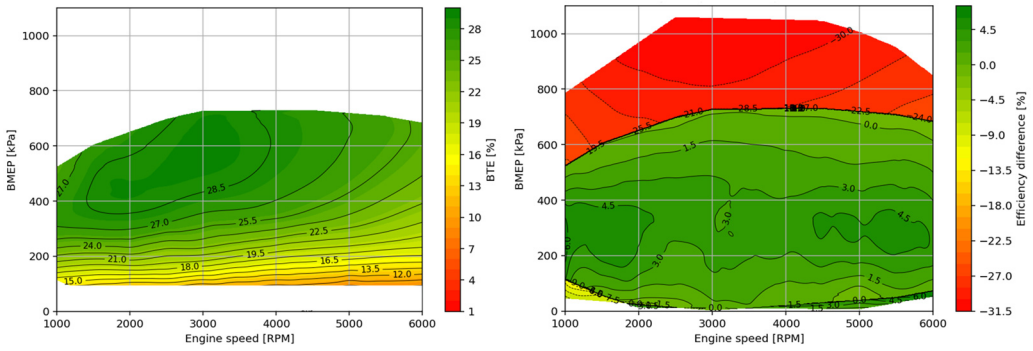


Figure 9. (**a**) Brake thermal efficiency map of the hydrogen-fueled SI engine. (**b**) Efficiency-difference map relative to gasoline operation, showing the regions of improved performance under lean hydrogen combustion.

Figure 9b highlights the difference in efficiency between both fuels, revealing gains of up to 4–5% in the most favorable zones, mainly at partial loads and moderate speeds. These improvements are attributed to hydrogen's faster flame speed, shorter combustion duration, and reduced heat losses at lean conditions. Nevertheless, the model also predicts a loss of maximum power output, driven by the lower air-filling and energy density of the mixture. This power loss is clearly highlighted in red in the figure, as the gasoline model exhibits higher output, with efficiency defined as the difference. However, it is noteworthy that at points where both engines operate, the hydrogen engine produces higher power. The numerical calibration demonstrates that the GT-SUITE predictive model successfully reproduces the expected efficiency trends of the retrofitted engine. This capability allows

identifying the thermodynamic potential and performance limitations of the hydrogen conversion before experimental modifications, providing a powerful tool for guiding real test-bench adjustments and evaluating retrofit strategies.

3.3. Hydrogen Conversion Kit and Operational Cost

The results from the numerical model were used to design a practical hydrogen conversion kit for the SI engine and to assess the associated operational costs. The simulations allowed identifying the key subsystems to adapt—injectors, ignition, throttle control, and electronic management—and quantifying the flow and mixture parameters required for stable hydrogen operation.

Figure 10 summarizes the main calibration maps derived from the model. Figure 10a shows the predicted mixture dilution across the speed–load range, confirming the predominance of lean operation (λ = 1.4–2.6) except at high loads, where near-stoichiometric mixtures are required to maintain torque output. Figure 10b displays the average hydrogen mass flow through the injector, which increases with load and speed, reaching up to 0.35 g/s per injector at 6000 rpm under stoichiometric conditions. This information provides the baseline for injector sizing and fuel delivery system design. The throttle-position map in Figure 10c illustrates the high sensitivity of air control at partial loads, where precise regulation of the intake airflow is needed to maintain the target lambda and avoid misfire. At high loads, the throttle remains nearly wide open, and mixture control depends solely on fuel injection. Therefore, the adoption of an electronic throttle body is recommended for improved accuracy and safety. Similarly, Figure 10d shows the spark-advance map, which was optimized to balance combustion stability and pressure-rise rate. Advance values between 10° and 50° CA bTDC were found suitable across the operating range, ensuring efficient energy conversion without exceeding the BarCAD limits defined previously.

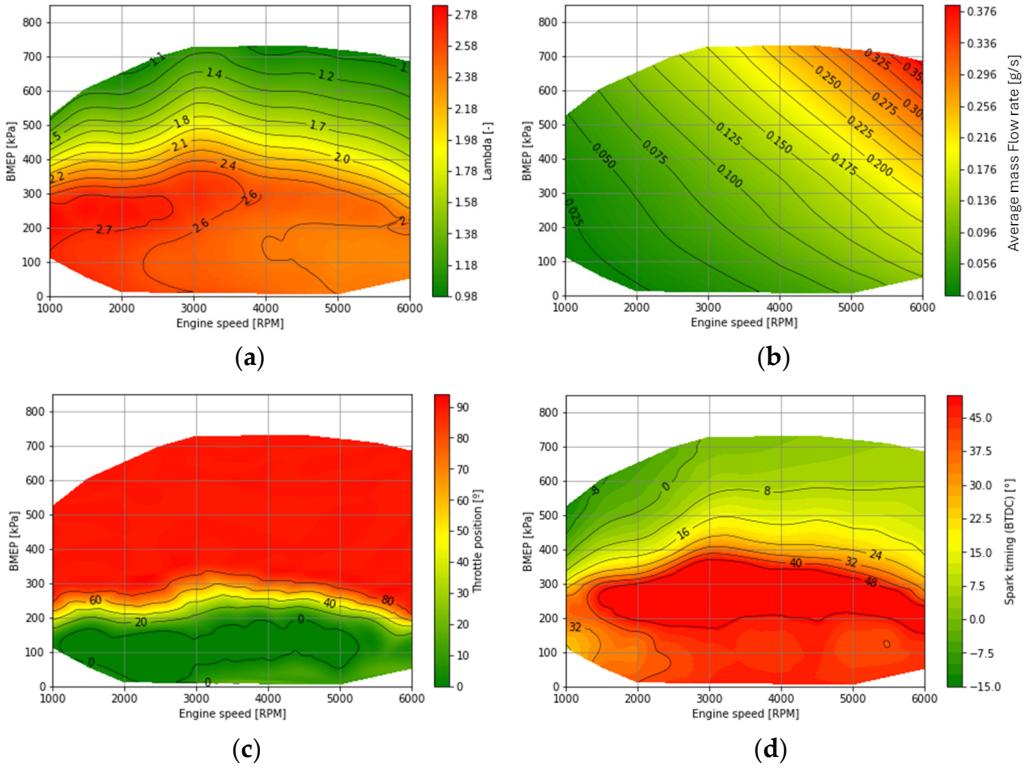


Figure 10. Numerical performed maps of the hydrogen engine: (**a**) mixture dilution (lambda); (**b**) average hydrogen flow rate through the injector; (**c**) throttle-valve position; (**d**) spark-advance distribution.

From a practical standpoint, the proposed conversion kit would include hydrogen-rated PFI injectors (e.g., Phinia Multec 3.5 H_2), cold-type spark plugs, an electronic throttle with pedal sensor, and a fully programmable ECU capable of managing sequential hydrogen injection and spark timing. All fuel lines, valves, and fittings must comply with hydrogen service standards to prevent leakage and material embrittlement.

An extensively discussed and analyzed issue is the formation of NO_x emissions in thermal engines, particularly in hydrogen engines operating near stoichiometric combustion. This occurs due to the large amount of nitrogen present in the intake air and the high flame temperatures. Several optimization studies have shown that, by carefully selecting the operating points, it is possible to significantly reduce these emissions without requiring substantial reductions in engine efficiency or power output [31]. Figure 11 compares the brake-specific NO_x emissions for gasoline (Figure 11a) and hydrogen (Figure 11b) across the full engine map. The predicted NO_x formation for hydrogen shows a clear dependence on the global equivalence ratio. Under stoichiometric conditions ($\lambda \approx 1.0$), hydrogen exhibits significantly higher NO_x production than gasoline due to its intrinsically higher adiabatic flame temperature and faster combustion rates, which intensify thermal-NO formation through the extended Zeldovich mechanism. This effect is most evident at medium-to-high loads (BMEP > 500 kPa) and moderate speeds (2500–4000 rpm), where the hydrogen contour map shows pronounced NO_x peaks exceeding 40 g/kWh. However, lean operation dramatically alters the NO_x trend. When the air–fuel ratio is increased ($\lambda \geq 2.0$), the combination of reduced burned-gas temperatures and the high dilution tolerance of hydrogen leads to a strong suppression of thermal NO. As shown in Figure 11b, the NO_x contours collapse to values below 10 g/kWh across most of the load-speed domain, with near-zero emissions at light loads (BMEP < 250 kPa). Quantitatively, lean hydrogen operation reduces NO_x by 65–80% relative to stoichiometric hydrogen operation, and by 40–60% when compared to gasoline at similar load conditions. These trends align with the expected thermochemical behavior of hydrogen flames and reinforce the suitability of excess-air strategies for minimizing NO_x formation in retrofitted hydrogen PFI engines.

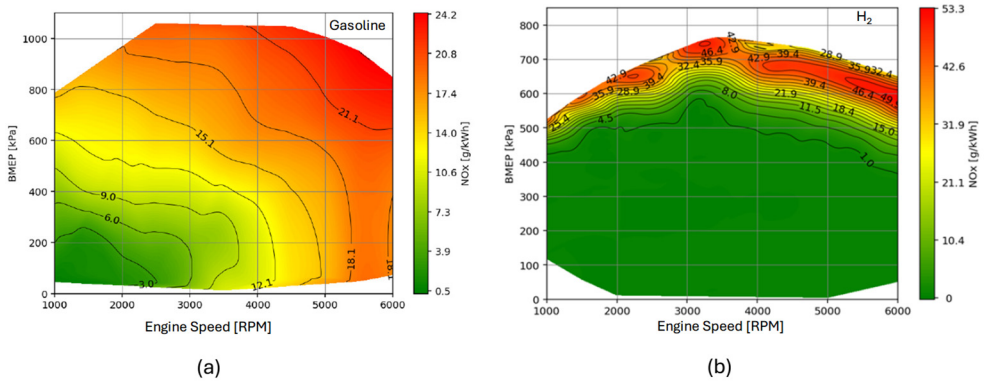


Figure 11. NO_x emissions predicted by numerical model for gasoline (**a**) and hydrogen (**b**) engine versions.

The equivalent hydrogen price was obtained by comparing the simulated fuel consumption of both gasoline and hydrogen operation at identical engine speed and load points. This value represents the hydrogen cost that would equalize the hourly fuel expenditure between the two fuels. The calculation followed the expression in Equation (4).

$$P_{H_2}\left[\frac{\$}{kg}\right] = 1000 \cdot \frac{P_{gasoline}\left[\frac{\$}{L}\right] \cdot BSFC_{gasoline}\left[\frac{g}{kWh}\right]}{BSFC_{H_2}\left[\frac{g}{kWh}\right] \cdot \rho_{gasoline}\left[\frac{g}{L}\right]} \quad (4)$$

where $P_{gasoline}[\$/L]$ denotes the retail gasoline price converted for this case from Uruguayan gasoline of 1.9 $\$/L$, $\rho_{gasoline}$ of 735 $[g/L]$. The BSFC values for both fuels were extracted from steady-state simulations at matched operating conditions. The resulting BSFC map defines, for each combination of speed and BMEP, the hydrogen price that achieves parity in fuel cost per unit of useful brake power.

Across most of the operating range, the equivalent hydrogen price required to achieve parity in hourly fuel cost with gasoline lies between 6 and 11 USD/kg, as illustrated in Figure 12. The lowest values—approaching 5 USD/kg—are concentrated around medium loads and moderate engine speeds (approximately 2000–3000 rpm), where the hydrogen engine exhibits its highest brake thermal efficiency. In contrast, the equivalent price increases sharply at high-speed and high-load conditions, reaching values above 13 USD/kg, primarily due to the rich mixtures and reduced volumetric efficiency associated with port fuel injection of hydrogen. These regions, however, represent a relatively small portion of typical driving operations. Considering current international projections for large-scale green hydrogen production, expected to fall below 5 USD/kg in the medium term [14], the analysis indicates that hydrogen retrofits could achieve cost competitiveness with gasoline engines in most real-world scenarios. The results highlight the strong influence of engine efficiency on the economic viability of hydrogen use: improvements in mixture formation, combustion control, and turbocharging strategies would further expand the cost-competitive region of the map. Although a moderate reduction in maximum power output is expected because of the displacement of intake air by the injected hydrogen, the gain in thermal efficiency and reduction in operating cost reinforce the potential of this concept as a practical and transitional pathway toward low-carbon internal combustion technologies. Moreover, coupling the system with on-site or renewable hydrogen supply could further enhance its sustainability and mitigate energy import dependence.

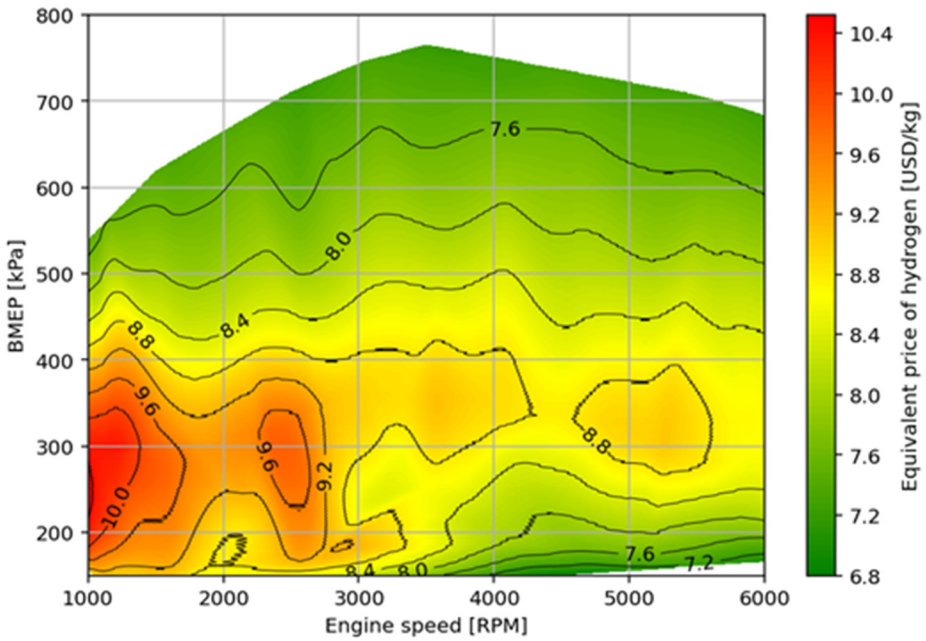


Figure 12. Equivalent hydrogen price map for cost parity with gasoline operation, derived from BSFC comparison between fuels.

When contextualized with current international fuel markets, the parity levels obtained in Uruguay are comparable to, or slightly above, the ranges reported in major economies. In Europe, retail gasoline prices typically oscillate between 1.7 and 2.1 USD/L, which, when inserted in the same formulation, shifts the hydrogen parity window upward

to approximately 5.5–10 USD/kg. In the United States, where gasoline averages around 1.0 USD/L, the corresponding hydrogen parity falls near 4–7 USD/kg, highlighting the stronger competitiveness required for hydrogen under lower-fuel-price contexts. Meanwhile, China—with retail gasoline near 1.1 USD/L and ambitious hydrogen deployment programs—shows an equivalent parity threshold around 4.5–6.5 USD/kg. These cross-regional comparisons confirm that large-scale hydrogen production costs projected between 3 and 5 USD/kg for green pathways (solar or wind-based electrolysis) [32] would allow hydrogen retrofits to achieve economic parity in all three markets.

It is interesting to compare the potential fuel savings with the cost of the conversion. To avoid an overly broad cost range and improve the transparency of the economic assessment, this work adopts a single representative cost for the hydrogen retrofit. Based on the component-level analysis performed in this study, which includes hydrogen-dedicated port injectors (e.g., Multec 3.5 H_2), cold-type spark plugs, a programmable ECU, an electronic throttle body and pedal assembly, pressure and temperature sensors for the storage system, a complete hydrogen supply line with fittings and safety accessories, and a dual-tank configuration to ensure minimum driving autonomy, the overall conversion cost converges to approximately 8000 USD. This value reflects the sum of all mandatory hardware required for a safe and functional hydrogen conversion in a small-displacement spark-ignition engine and corresponds to a realistic workshop-based retrofit performed on an existing vehicle platform. Optional elements—such as larger or additional storage tanks to increase range—can increase total cost, but they do not affect the baseline configuration analyzed here. For this reason, a unique representative cost yields a more robust and tractable comparison between gasoline and hydrogen operation, while remaining grounded in the detailed hardware requirements identified in this work.

4. Conclusions

This work uses a one-dimensional numerical model to study the thermodynamic and combustion behavior of a hydrogen-retrofitted spark-ignition engine. The integrated experimental–numerical methodology allowed a robust calibration of the Geely MR479Q engine for gasoline operation. The hydrogen retrofitting was predicted with one-dimensional combustion models. Key physical constraints, such as maximum in-cylinder pressure and pressure rise rate (bar/°CA), were captured. The predictive approach based on GT-SUITE enabled efficient identification of the optimal operating envelope, defining both the minimum and maximum lambda limits, and provided a clear understanding of the trade-offs between mixture dilution, combustion stability, and efficiency. This methodology proved valuable for anticipating the effects of hydrogen fueling prior to hardware modification, reducing experimental effort and risk during conversion.

The simulation results showed that hydrogen operation leads to higher brake thermal efficiencies than gasoline across most of the load range, with improvements of up to 5% in the mid-load region. These gains are attributed to hydrogen's faster flame speed and wider flammability range, which allow ultra-lean combustion and reduced heat losses. However, the retrofitted engine experiences a decline in volumetric efficiency and maximum power output due to the air-displacement effect inherent to port fuel injection (PFI). This limitation could be overcome with the implementation of direct hydrogen injection (DI), which would preserve the air charge, increase the attainable torque, and further expand the high-efficiency region. The model calibration also enabled the development of detailed maps for spark timing, injector flow, and throttle control—providing a solid basis for real-engine testing and ECU configuration.

From a techno-economic perspective, the study defined a complete hydrogen conversion kit and assessed its operational cost using simulation-based fuel-consumption

data. The analysis revealed that hydrogen engines can reach cost parity with gasoline operation when the hydrogen price falls below approximately 5–6 USD/kg, a range aligned with near-term green-hydrogen projections. Overall, the findings confirm that hydrogen retrofitting constitutes a technically and economically viable intermediate pathway toward low-carbon mobility, combining improved efficiency, local adaptability, and the progressive decarbonization of internal-combustion technologies.

Although DI is widely recognized as an effective strategy to recover volumetric efficiency in hydrogen engines, the present study focuses exclusively on PFI operation, consistent with the hardware layout of the base MR479Q engine. Several experimental and numerical works have previously demonstrated the benefits of DI for hydrogen combustion, and the optimization of DI strategies will be addressed in a dedicated future study.

Author Contributions: Conceptualization, S.B.-I., S.M.-B. and A.I.; methodology, S.B.-I., F.R. and S.M.; software, S.B.-I. and B.F.; validation, S.M.-B., F.R., B.F. and A.I.; formal analysis, S.B.-I. and S.M.; investigation, S.B.-I., F.R. and S.M.; resources, S.M.-B. and A.I.; data curation, S.B.-I. and B.F.; writing—original draft preparation, S.B.-I.; writing—review and editing, S.M.-B., S.M. and A.I.; visualization, S.B.-I. and B.F.; supervision, S.M.-B. and A.I.; project administration, S.M.-B.; funding acquisition, S.M.-B. All authors have read and agreed to the published version of the manuscript.

Funding: This research received no external funding.

Data Availability Statement: The data supporting the findings of this study, including the GT-SUITE simulation files and experimental measurements from the IIMPI engine test bench, are available from the corresponding author upon reasonable request. Restrictions apply to the availability of these data due to institutional policies and ongoing research activities.

Conflicts of Interest: The authors declare no conflicts of interest.

Abbreviations

The following abbreviations are used in this manuscript:

BMEP	Brake Mean Effective Pressure
BSFC	Brake Specific Fuel Consumption
BTE	Brake Thermal Efficiency
CAD	Crank Angle Degree
DoE	Design of Experiments
DI	Direct Injection
ECU	Engine Control Unit
GT	Gamma Technologies (GT-SUITE software)
H_2	Hydrogen
ICE	Internal Combustion Engine
λ (Lambda)	Air–Fuel Equivalence Ratio
NO_x	Nitrogen Oxides
PFI	Port Fuel Injection
PMS/TDC	Punto Muerto Superior/Top Dead Center
rpm	Revolutions Per Minute
SI	Spark Ignition
SITurb	Spark-Ignition Turbulent Combustion Model
USD	United States Dollar
Udelar	Universidad de la República
WOT	Wide-Open Throttle

References

1. El-Adawy, M.; Nemitallah, M.A.; Abdelhafez, A. Towards sustainable hydrogen and ammonia internal combustion engines: Challenges and opportunities. *Fuel* **2024**, *364*, 131090. [CrossRef]
2. Raugei, M.; Winfield, P. Prospective LCA of the production and EoL recycling of a novel type of Li-ion battery for electric vehicles. *J. Clean. Prod.* **2019**, *213*, 926–932. [CrossRef]
3. Escalante Soberanis, M.A.; Fernandez, A.M. A review on the technical adaptations for internal combustion engines to operate with gas/hydrogen mixtures. *Int. J. Hydrogen Energy* **2010**, *35*, 12134–12140. [CrossRef]
4. Lu, Y.; Que, J.; Xia, Y.; Li, X.; Jiang, Q.; Feng, L. A comparative study of the effects of EGR on combustion and emission characteristics of port fuel injection and late direct injection in hydrogen internal combustion engine. *Appl. Energy* **2024**, *375*, 123830. [CrossRef]
5. Silveira, J.P.; Fagundez, J.L.S.; Garlet, R.A.; Martins, M.E.S.; Salau, N.P.G.; Lanzanova, T.D.M. International Journal of Hydrogen Energy Hydrogen-fueled PFI SI engine investigation for near-zero NO x emissions in de-throttled and supercharged ultra-lean burn conditions. *Int. J. Hydrogen Energy* **2024**, *91*, 800–813. [CrossRef]
6. Lago Sari, R.; Fogue Robles, A.; Monsalve Serrano, J.; Cleary, D. Techno-economic assessment of hydrogen as a fuel for internal combustion engines and proton exchange membrane fuel cells on long haul applications. *Energy Convers. Manag.* **2024**, *311*, 118522. [CrossRef]
7. Lou, D.; Chen, G.; Zhang, Y.; Fang, L.; Tan, P.; Hu, Z. Single-factor analysis and multi-objective optimization of hydrogen injection strategies and stoichiometric control for a PFI hydrogen ICE. *J. Clean. Prod.* **2025**, *534*, 147126. [CrossRef]
8. Ji, C.; Wang, S. Effect of hydrogen addition on the idle performance of a spark ignited gasoline engine at stoichiometric condition. *Int. J. Hydrogen Energy* **2009**, *34*, 3546–3556. [CrossRef]
9. Bibiloni-Ipata, S.; Vielmo-Cogo, V.; Frizzo-Prante, G.; Martinez-Boggio, S. Design and study of the effects of retrofitting diesel engines in hydrogen trucks through simulation. *Int. J. Hydrogen Energy* **2025**, *163*, 150806. [CrossRef]
10. Barış, O.; Güler, İ.; Yaşgül, A. The effect of different charging concepts on hydrogen fuelled internal combustion engines. *Fuel* **2023**, *343*, 127983. [CrossRef]
11. Wittek, K.; Cogo, V.; Prante, G. Full load optimization of a hydrogen fuelled industrial engine. *Int. J. Hydrogen Energy* **2024**, *77*, 230–243. [CrossRef]
12. Ma, D.S.; Sun, Z.Y. Progress on the studies about NO_x emission in PFI-H2ICE. *Int. J. Hydrogen Energy* **2020**, *45*, 10580–10591. [CrossRef]
13. Helgeson, B.; Peter, J. The role of electricity in decarbonizing European road transport—Development and assessment of an integrated multi-sectoral model. *Appl. Energy* **2020**, *262*, 114365. [CrossRef]
14. IRENA. *GREEN HYDROGEN COST REDUCTION: Scaling Up Electrolysers to Meet the 1.5 °C Climate Goal*; IRENA: Abu Dhabi, United Arab Emirates, 2020.
15. Qi, Y.; Liu, W.; Liu, S.; Wang, W.; Peng, Y.; Wang, Z. A review on ammonia-hydrogen fueled internal combustion engines. *ETransportation* **2023**, *18*, 100288. [CrossRef]
16. Liang, Z.; Xie, F.; Wang, Z.; Lu, C.; Su, Y.; Li, X.; Jiang, B.; Guo, Z. Suppressing pre-ignition and knock in hydrogen direct injection spark ignition engines with variable valve timing and split injection. *Energy Convers. Manag.* **2025**, *327*, 119570. [CrossRef]
17. Park, H.; Lee, J.; Oh, S.; Kim, C.; Park, Y. Strategies of hydrogen-air mixture formation for suppressing backfire, pre-ignition, and knock in full-load operations of hydrogen heavy-duty engines. *Energy* **2025**, *326*, 136343. [CrossRef]
18. Zhang, W.; Wang, Y.; Long, W.; Tian, H.; Dong, P. International Journal of Hydrogen Energy Numerical investigation on knock intensity, combustion, and emissions of a heavy-duty natural gas engine with different hydrogen mixing strategies. *Int. J. Hydrogen Energy* **2024**, *62*, 551–561. [CrossRef]
19. Gamma Technologies, Inc. *GT-SUITE: Engine and System Simulation Software*; Gamma Technologies: Westmont, IL, USA, 2024. Available online: https://www.gtisoft.com/gt-suite/ (accessed on 7 December 2020).
20. Demesoukas, S.; Brequigny, P.; Caillol, C.; Halter, F.; Mounaïm-Rousselle, C. 0D modeling aspects of flame stretch in spark ignition engines and comparison with experimental results. *Appl. Energy* **2016**, *179*, 401–412. [CrossRef]
21. Curto-Risso, P.L.; Medina, A.; Hernández, A.C. Theoretical and simulated models for an irreversible Otto cycle. *J. Appl. Phys.* **2008**, *104*, 094911. [CrossRef]
22. Michl, J.; Neumann, J.; Rottengruber, H.; Wensing, M. Derivation and validation of a heat transfer model in a hydrogen combustion engine. *Appl. Therm. Eng.* **2016**, *98*, 502–512. [CrossRef]
23. Teodosio, L.; Pirrello, D.; Berni, F.; De Bellis, V.; Lanzafame, R.; D'Adamo, A. Impact of intake valve strategies on fuel consumption and knock tendency of a spark ignition engine. *Appl. Energy* **2018**, *216*, 91–104. [CrossRef]
24. Nagappa, M.; Hebbur Rameshbabu, A. Comparison of Predictive Gasoline Combustion Models Using GT-Power. Master's Thesis, Chalmers University of Technology, Göteborg, Sweden, 2016.

25. Merola, S.S.; Di Iorio, S.; Irimescu, A.; Sementa, P.; Vaglieco, B.M. Spectroscopic characterization of energy transfer and thermal conditions of the flame kernel in a spark ignition engine fueled with methane and hydrogen. *Int. J. Hydrogen Energy* **2017**, *42*, 13276–13288. [CrossRef]
26. Italy. *A Comparison Between Two Phenomenological Combustion Models Applied to Different SI Engines*; SAE: Warrendale, PA, USA, 2017.
27. Ayala, F.A.; Heywood, J.B. *Lean SI Engines: The Role of Combustion Variability in Defining Lean Limits*; Sloan Automotive Laboratory, Massachusetts Institute of Technology: Cambridge, MA, USA, 2007; Volume 21. [CrossRef]
28. Demesoukas, S.; Caillol, C.; Higelin, P.; Boiarciuc, A. Zero-Dimensional Spark Ignition Combustion Modeling—A Comparison of Different Approaches. In Proceedings of the 11th International Conference on Engines & Vehicles, Napoli, Italy, 15–19 September 2013. [CrossRef]
29. Verhelst, S.; Maesschalck, P.; Rombaut, N.; Sierens, R. Increasing the power output of hydrogen internal combustion engines by means of supercharging and exhaust gas recirculation. *Int. J. Hydrogen Energy* **2009**, *34*, 4406–4412. [CrossRef]
30. Swain, M.R.; Pappas, J.M.; Adt, R.R., Jr.; Escher, W.J.D. Hydrogen-fueled automotive engine experimental testing to provide an initial design-data base. *SAE Tech. Pap.* **1981**, 810350. [CrossRef]
31. Zhao, F.C.; Sun, B.G.; Yuan, S.; Bao, L.Z.; Wei, H.; Luo, Q.H. Experimental and modeling investigations to improve the performance of the near-zero NO_x emissions direct-injection hydrogen engine by injection optimization. *Int. J. Hydrogen Energy* **2024**, *49*, 713–724. [CrossRef]
32. Hydrogen Council, McKinsey & Company. *Hydrogen Insights A Perspective on Hydrogen Investment, Market Development and Cost Competitiveness*; Hydrogen Council, McKinsey & Company: Belgium, Brussels, 2021.

Disclaimer/Publisher's Note: The statements, opinions and data contained in all publications are solely those of the individual author(s) and contributor(s) and not of MDPI and/or the editor(s). MDPI and/or the editor(s) disclaim responsibility for any injury to people or property resulting from any ideas, methods, instructions or products referred to in the content.